Materials Horizons

Upcycling of mixed polyolefin wastes to 3D structured carbon Joule heaters for decarbonized hydrogen production

Journal:	*Materials Horizons*
Manuscript ID	MH-COM-12-2024-001755.R1
Article Type:	Communication
Date Submitted by the Author:	11-Feb-2025

Complete List of Authors:	Griffin, Anthony; University of Southern Mississippi, School of Polymer Science and Engineering Wu, Jiachun; Mississippi State University, Dave C. Swalm School of Chemical Engineering Smerigan, Adam; The Pennsylvania State University, Chemical Engineering Smith, Paul; University of Southern Mississippi, School of Polymer Science and Engineering Adedigba, Gbadeoluwa; University of Southern Mississippi Shi, Rui; The Pennsylvania State University, Chemical Engineering Xiang, Yizhi; Mississippi State University; University of Missouri Columbia, Department of Chemical and Biomedical Engineering Qiang, Zhe; University of Southern Mississippi

New Concept:

Significant progress has been made in converting polyolefin waste into fuels and chemicals, but the environmental benefits are often offset by added costs and emissions from upcycled products. To address this challenge, we demonstrate a simple chemical transformation that converts 3D-printed plastic waste into catalytic reactors with exceptional Joule heating capabilities for distributed hydrogen production via ammonia decomposition. The resulting carbon-based Joule heaters enable rapid, on-demand reaction control and significantly enhanced conversion rates compared to conventional thermal methods, leveraging the benefits of electrical current. Life cycle assessments reveal that, when powered by renewable energy sources like wind and solar, this approach achieves near-zero-emission hydrogen production, offering a transformative step toward sustainable energy solutions.

Data Availability Statement

The data supporting this article have been included as part of the Supplementary Information.

Upcycling of mixed polyolefin wastes to 3D structured carbon Joule heaters for decarbonized hydrogen production

Anthony Griffin,[a] Jiachun Wu,[b] Adam Smerigan,[c] Paul Smith,[a] Gbadeoluwa Adedigba,[a] Rui Shi,[c] Yizhi Xiang,[b,d,*] Zhe Qiang[a,*]

[a]School of Polymer Science and Engineering, University of Southern Mississippi, Hattiesburg, MS, 39406, USA

[b]Dave C. Swalm School of Chemical Engineering, Mississippi State University, MS State, MS, 39762, USA

[c]Department of Chemical Engineering, The Pennsylvania State University, University Park, PA, USA

[d]Department of Chemical and Biomedical Engineering, University of Missouri, Columbia, MO, 65211, USA

Corresponding authors: Y.X. (yxpxb@missouri.edu); Z. Q. (zhe.qiang@usm.edu)

Abstract

Societal decarbonization is essential for environmental sustainability and prosperity, requiring cohesive efforts to advance materials circularity alongside the development of zero-carbon energy and heat solutions. In most systems, these challenges are addressed separately. However, creating integrated solutions that connect opportunities across energy and materials loops can be transformative and critical for achieving lasting impact. This work shows the innovative use of mixed polyolefin wastes for electrification of heating to enable industrial decarbonization. We demonstrate the conversion of mixed polyolefin wastes into structured carbon with exceptional Joule heating properties using fused filament fabrication (FFF) printing, crosslinking, and pyrolysis. This waste-derived carbon serves as both a catalyst support and heating element for electrified hydrogen production via NH_3 decomposition. This Joule heating-enabled process leads to enhanced intrinsic catalytic activity and demonstrates accelerated reaction start and shutdown speeds compared to the convection heating method, while having the advantage of reducing global warming and life cycle energy consumption impacts. By simultaneously upcycling mixed plastic waste and enabling hydrogen production through energy-efficient processes, this work presents a robust and integrated pathway toward industrial decarbonization.

Keywords: Electrified chemical synthesis, waste resource management, life cycle assessment, resistive heating, additive manufacturing

1. Introduction

The long-term health of our planet and the well-being of future generations rely on achieving both environmental preservation and economic prosperity. Achieving these goals requires efforts in reducing greenhouse gas emissions (GHGs), improving resource efficiency,

and developing carbon-neutral energy solutions, all working in unison to combat climate change and drive the adoption of a decarbonized economy. While there are numerous efforts to address materials circularity and zero-carbon energy—both essential to industrial decarbonization—these challenges are often tackled separately. For instance, in the critical area of mixed plastic recycling,[1,2] particularly with polyethylene (PE) and polypropylene (PP), significant progress has been made in converting polyolefin waste into valuable chemicals and fuels or developing compatibilization strategies.[3–8] While these methods show promise, the sequential use of upcycled products often results in added costs and emissions, complicating the process and potentially offsetting some of the environmental benefits gained. Meanwhile, the global adoption of hydrogen as a renewable, carbon-free energy carrier faces significant hurdles due to its high energy requirements in synthesis, which often lead to considerable greenhouse gas (GHG) emissions, as well as difficulties in its storage and transportation.[9] While ammonia (NH_3) has been identified as a leading hydrogen carrier candidate due to its historical usage and existing infrastructure, as well as its high hydrogen content (17 wt%),[10,11] their decomposition for hydrogen production is a highly endothermic reaction.[12] In these processes, conventional fossil fuel-fired and external heated reactors not only lead to significant GHG emission but also create large thermal gradients, resulting in significant heat loss, and poor catalyst utilization. To address these systemic issues, integrated solutions that simultaneously advance both waste circularity and decarbonized energy production are essential to unlock the potential of largely underexplored waste streams and accelerate the transition to a hydrogen economy, ultimately reducing the overall environmental footprint.

Furthermore, electrifying heating processes is key to decarbonizing chemical and energy production, while enabling the seamless integration of renewable energy sources to power these processes.[13,14] For example, the electrification of steam methane reforming can lead to significant process intensification,[15,16] enabling compact reactors that are approximately 100 times smaller than conventional platforms. Moreover, a carbon felt coated with Fe or Ru catalysts was employed for the synthesis of NH_3 with rapid pulsed Joule heating,[17] resulting in high reaction rates (up to 4000 μmol g_{Fe}^{-1} h^{-1}) and high catalyst stability. It is worth noting that Ru-loaded carbon supports have also been utilized for hydrogen production through electrocatalytic hydrogen evolution reactions as an alternative to steam methane reforming and ammonia decomposition strategies.[18–22] Similarly, carbon fiber paper can be used for dry methane reforming with a rapid pulsed heating strategy,[23] leading to enhanced methane conversion. Recent works also demonstrate the robust use of Joule heating methods to synthesize functional nanomaterials from low-value precursors, such as graphene,[24,25] metal oxides,[26] and metal carbides.[27] These works showcase significant advances in electrified chemical syntheses using carbon supports as Joule heaters,[28,29] but a major challenge still remains associated with the lack of ability to enable customized and optimal reactor designs, which limits the broader applicability and scaling up of industrial electrification strategies. While recent works show additive manufacturing (AM) of carbon using polyolefin precursors,[30,31] which exhibit excellent Joule heating properties, their potential in decarbonized chemical synthesis remains untapped.

This work addresses a pressing need to develop technologies for decarbonized chemical synthesis (green H_2 production from NH_3 decomposition) via innovative upcycling of mixed polyolefin waste. By using low-value waste PP/PE blends as feedstock, the resulting carbons can simultaneously function as heaters and catalyst supports for hydrogen production through NH_3 decomposition, capitalizing on their exceptional Joule heating performance and chemical stability. Electrified hydrogen production achieves higher conversions and faster reaction start and

shutdown speeds compared to their counterpart using convectional heating. Moreover, life cycle analysis shows this Joule heating approach lowers GHG as well as life cycle energy consumption (LCEC) compared to conventional furnace heating, resulting in reduced environmental footprint as we transition to more renewable energy sources. Together, this work offers a very promising solution to simultaneously address several key sustainability challenges, including mixed plastic waste upcycling, AM of Joule heaters, and carbon-zero energy production through electrified chemical synthesis, which can be an integral component toward a decarbonized society.

2. Experimental Section

2.1 Materials preparation

A series of mixed polyolefin waste systems were investigated, including a commercial 3D filament (Braskem FL600R, primarily PE) and several in-house prepared blends with varying PE/PP compositions. Specifically, the commercial filament was purchased from Xtellar with a diameter of 2.85 mm, primarily sourced from recycled bottle caps composed of approximately 90% sustainably sourced material. In addition, three PE/PP blend compositions (including 20 wt% PP, 40 wt% PP, and 80 wt% PP) of waste-derived 3D printing filament was prepared by collecting PP and PE wastes from disposed cups, followed by grinding and compounding them with a Filabot single screw extruder with a puller at a nozzle temperature of 225 °C and screw speed of 10 rpm.

Carbon-based catalyst supports were prepared using recycled polyolefin blends as precursors and a fused filament fabrication (FFF) printer (Ultimaker S3), where a model system of a cylinder with 10 mm height, 12.5 mm diameter, and an inner hole with a 2.5 mm diameter was used. The structure was printed with no top or bottom layers and an infill percentage of 60% with a grid pattern to increase the density of the cross section. To briefly describe the printing procedure, a nozzle temperature of 225 °C and a printing bed temperature of 60 °C was used (note a printing bed temperature of 110 °C was used for establishing the initial layer), and Magigoo adhesive was applied onto the printing bed to prevent warping of printed parts. 3D structures were printed with 20% fan speed and 40 mm/s printing speed along with a brim and with the absence of support material. Additional structures were also prepared with identical printing parameters as the model system. STL files for the complex structures reported in this study can be found on Thingiverse.com.

After 3D printing, mixed polyolefin parts were converted to carbon through the following procedure. Briefly, printed parts were placed into 100 mL glass beakers and 50 mL of concentrated sulfuric acid (98%; purchased from Sigma Aldrich) was added to the reaction vessel. A 25 mL beaker was placed on top of the printed samples to ensure full submersion of printed parts in acid throughout the entire reaction. The vessel was then placed in a Thermo Scientific Thermolyne F6010 muffle furnace and heated to various temperatures (115-145 °C) with varied amounts of time (2-72 h) for sulfonation and crosslinking of printed parts. Subsequently, samples were then removed from the furnace and cooled to room temperature, followed by washing with deionized (DI) water (Millipore Sigma Milli-Q IQ 7003) at least three times in order to remove any residual acid and reaction byproducts. Washed samples were then dried overnight under vacuum at 50 °C. Fully dried species were carbonized using an Across international TF1400 tube furnace with a ramp rate of 1 °C/min up to 600 °C, followed by a rate of 5 °C/min until 800 °C under a nitrogen environment.

The 3D printed carbon cylinder was then treated with NH_3 before impregnating catalytically active Ru species. The NH_3 treatment was carried out in a 0.5 inch diameter quartz tube by

heating the sample at a ramp of 10 °C/min to 800 °C and held for 6 h under 20 mL/min of NH_3. The sample was then cooled to room temperature under NH_3 atmosphere. Subsequently, Ru was introduced into the pretreated carbon cylinder through incipient wetness impregnation with ruthenium(III) chloride ($RuCl_3$, Millipore Sigma) as the precursor, and followed by reduction in the liquid phase by sodium borohydride ($NaBH_4$ (98%, thermo scientific)). Specifically, the required amounts of $RuCl_3$ solution (around 0.4 mL) were added dropwise into the 3D printed carbon to achieve a nominal Ru loading of 1 wt%. The sample was impregnated for 2 h under ambient conditions and then reduced with excessive $NaBH_4$ aqueous solution (molar ratio of $NaBH_4$ to $RuCl_3$ is approximately 10:1) under ambient conditions. After the reduction reaction, the sample was rinsed with water 3 times to remove residual impurities. The obtained sample was finally dried at 100 ºC for 12 h before the Joule heating catalytic NH_3 decomposition evaluation.

2.2 Sample physical characterization

The degree of crosslinking was examined through gel fraction experiments, where sulfonated samples were placed in hot xylene at 120 °C for 24 h, and the change in mass was used to determine the insoluble fraction as shown in the following equation:

$$Gel\ fraction = \frac{m_d}{M_i} * 100 \quad (1)$$

where m_i is the weight of sample before extraction and m_d is the weight of sample following extraction. A Discovery 250 (TA instruments) was used for differential scanning calorimetry (DSC) experiments, and the degree of PE and PP crystallinity was determined using the melting peak from the second heating cycle, which was compared to the theoretical melting enthalpy of PE (~293 J/g) and PP (~209 J/g).[32,33] An initial heating cycle from 20 °C to 200 °C with a 10 °C/min heating rate was employed to erase thermal history. Samples were then cooled with a 5 °C/min cooling rate to 20 °C, followed by heating back to 200 °C at 10 °C/min. Data analysis was performed with Trios software. The carbon yield of 3D printed parts was determined by comparing the mass of the initial printed structure with the final carbon, while the dimensional shrinkage was determined by comparing the critical dimensions of the final carbon to the initial printed structure.

A Zeiss Ultra 60 field-emission scanning electron microscope (SEM) was used to examine the morphological changes of printed structures throughout the crosslinking and carbonization steps, with an accelerating voltage of 12 kV. Samples were sputter coated with carbon prior to imaging using a 208 Cressington Carbon Coater. Liquid nitrogen physisorption measurements were conducted with a Micromeritics Tristar II 3020 at 77K to further assess the pore textures of carbonaceous species, including pore size distributions (determined by non-local density functional theory with a carbon slit model) and surface areas (determined by Brunauer−Emmett−Teller model). A Thermo Fisher ESCALAB Xi+ spectrometer equipped with a monochromatic Al X-ray source (1486.6 eV) and a MAGCIS Ar+/Arn+ gas cluster ion sputter gun was used for X-ray photoelectron spectroscopy (XPS) experiments. Spectral acquisition was carried out with a base pressure of 3×10^{-7} mbar within the analysis chamber and a takeoff angle of 90° with respect to the surface. Avantage software from Thermo Fisher was used to fit high-resolution scans. Transmission electron microscopy (TEM) images were obtained using a JEOL 2100TEM (accelerating voltage 200 kV) equipped with a Gatan camera. X-ray powder diffraction (XRD) patterns were collected on a Rigaku Ultima III X-ray diffractometer with monochromatic Cu Kα radiation (154.06 pm, 40 kV, and 44 mA) with a scan speed of 4°/min.

2.3 Catalytic reaction studies

The Joule heating catalytic NH_3 decomposition was carried out in an in-house established Joule heating catalytic reactor consisting of a 0.5 inch diameter quartz tube with an inner diameter of 10 mm. The quartz reactor was wrapped with a 1 cm thickness of ceramic fiber to limit heat loss. The carbon cylinder joule heater/catalyst with the same diameter as the quartz tube was sandwiched between two conductive steel wool and loaded at the center of the quartz reactor. A 1/16 inch diameter copper rod and a K-type thermocouple were used as electrodes in contact with the steel wool. The tip of the thermocouple was inserted into the carbon cylinder for the bulk temperature measurement during the reaction (or under an inert atmosphere to measure the Joule heating performance). The electrodes from both sides of the reactor were connected to an Eventek DC Power Supply (30V/10A Variable Power Supply). The temperature of the catalyst was online monitored with a Platinum series universal benchtop temperature controller (Omega™ Engineering). The catalyst was in-situ activated at 550 °C for 30 min under 10% H_2/Ar (20 mL/min). After activation, the temperature was tuned to below 200 °C by decreasing the current passed through the carbon cylinder, and the reactor inlet was switched to undiluted NH_3 (at different flow rates depending on the desired space velocity). Then the by-pass NH_3 signal was measured by an online mass spectrometer (Leybold Inficon Transpector Residual Gas Analyzer TSP TH100). After the NH_3 signal (m/z = 16) became stable, the temperature of the carbon cylinder was tuned to 400 – 550 °C (by increasing the current) for NH_3 decomposition. The temperature was kept for at least 15 min until the reaction reached steady-state (the signals of m/z = 16 and m/z = 28 became stable). The MS signal intensities of NH_3 and N_2 were converted to partial pressure based on external standard calibration (partial pressure/intensity relationship). Finally, the mole flow rate of NH_3 and N_2 were calculated based on the ideal gas equation of state ($\mathrm{P_i v = F_i RT}$), where P_i is the partial pressure of selected molecules (Pa), v is the volumetric flow rate (mL/S) at the exit of the reactor, F_i is the mole flow rate (mol/S), R is the ideal gas constant (J/mol/K), and T is the temperature (K). NH_3 conversion (x) was calculated based on eq. (2).

$$x = \frac{F_{NH_3,\,in} - F_{NH_3,\,out}}{F_{NH_3,\,in}} \tag{2}$$

where $F_{NH_3,\,in}$ and $F_{NH_3,\,out}$ are the mole flow rate (mol/S) of NH_3 at the inlet and outlet of the reactor, respectively. Noteworthily, due to the change in the total number of moles in the NH_3 decomposition, the volumetric flow rate (v) was calculated based on eq. (3).

$$v = v_{in}(1 + x). \tag{3}$$

where v_{in} is inlet volumetric flow rate. The rate of H_2 production was calculated based on the mole flow rate of H_2 ($F_{H_2} = 1.5 \times (F_{NH_3,\,in} - F_{NH_3,\,out})$) following eq. (4).

$$Rate = \frac{F_{H_2}}{mass\ of\ carbon\ cylinder} \tag{4}$$

2.4 Life Cycle Assessment (LCA)

A Life Cycle Assessment (LCA) study was conducted to characterize the environmental impacts of Joule-heated NH_3 decomposition for hydrogen production, following International Standards Organization (ISO) 14040/14044 standards.[34,35] A functional unit of 1 kg of hydrogen produced was chosen to ensure equal function between Joule heating versus conventional furnace heating methods. The scope is defined as gate-to-gate, focusing only on the hydrogen conversion stage, as the impacts from other life cycle stages (e.g., ammonia production, recycling,

transportation, and distribution) are assumed to be equivalent between the two systems. The system boundary is shown in Figure S1. The carbon-based Joule heaters were prepared using recycled mixed polyolefin waste, so no material impacts were considered. If the avoided landfill impact was accounted for, the system has the potential to further reduce its overall environmental impact. Activities from the ecoinvent v3.9.1 cutoff database were used for the background inventory inputs.[36] Only life cycle impacts from heat and electricity generation were accounted for in this gate-to-gate LCA study. A full list of the specific activities used is provided in Table S1. The base case electric grid used in the analysis is the Energy Information Administration (EIA) 2020 average U.S. grid composition,[37] with other renewable grid mixes considered in the scenario analysis. For impact assessment, the US.EPA TRACI v2.1 characterization factors were used to characterize the environmental impact of both systems.[38] Additionally, the life cycle energy consumption (LCEC) was calculated using the Cumulative Energy Demand method to understand the primary energy usage of each system.[39]

The foreground life cycle inventory was calculated using the experimental data in Table S2-S5. The lab-scale conversion across a range of temperatures is provided in Table S2 for both the furnace and Joule heater. These conversions were used to calculate the production of hydrogen gas. To calculate the industrial-scale power consumption for the Joule heater, two different scenarios were used: the “base-case” scenario (BC scenario) and the “theoretical minimum” scenario (TM scenario). In the BC scenario, the power requirement is calculated using the experimentally measured values. The heat lost to the environment was subtracted and an industrially relevant heat efficiency was used to adjust power consumption.[40,41] The power consumption of the furnace was assumed to be the same as the BC Joule heater, except with a different industrial heat efficiency for losses to the environment (industrial heat efficiency of 80%).[42,43] In the TM scenario, the Joule heater power requirement was calculated as the sum of the heat required for reaction and for heating the feed stream. We note that this value was adjusted using industrially relevant heat efficiencies. Therefore, this TM scenario is optimistic and assumes that inefficiencies in the lab-scale system will be reduced as the technology develops to industrial-scale (e.g., Joule heater length increases decreasing losses from the electrodes). The methodology is described in more detail in Section S1.1 and Figure S2.

3. Results and Discussion

3.1. Fabrication of structured carbons from recycled mixed polyolefins

This work reports an innovative strategy to address mixed polyolefin waste and decarbonized hydrogen production *via* NH_3 decomposition. As shown in Scheme 1, mixed polyolefin wastes were first converted into structured carbons via steps of 3D printing and chemical transformations. We note that for polyolefin recycling, a key challenge is to address comingled, real-world polypropylene (PP)/polyethylene (PE) with varied compositions and the presence of additives, which is commonly present in waste streams due to the difficulty in their efficient separation and sorting. Importantly, mixed polyolefin wastes are a severely underutilized and challenging waste stream, as their phase separation can lead to very poor properties following mechanical reprocessing.[44] Subsequently, the waste-derived structured carbons can simultaneously serve as Joule heaters and catalyst supports. Through the introduction of catalytically active nanoparticles and the application of Joule heating, efficient decomposition of NH_3 can be achieved for decarbonized and distributed hydrogen production. In contrast to conventionally fired catalytic processes, this Joule heating-driven catalytic strategy not only allows the use of renewable sources as energy input but also enhances the catalytic efficiency due to the positive impact of electric current/field on the interactions between reactant/intermediates and the catalyst surface.

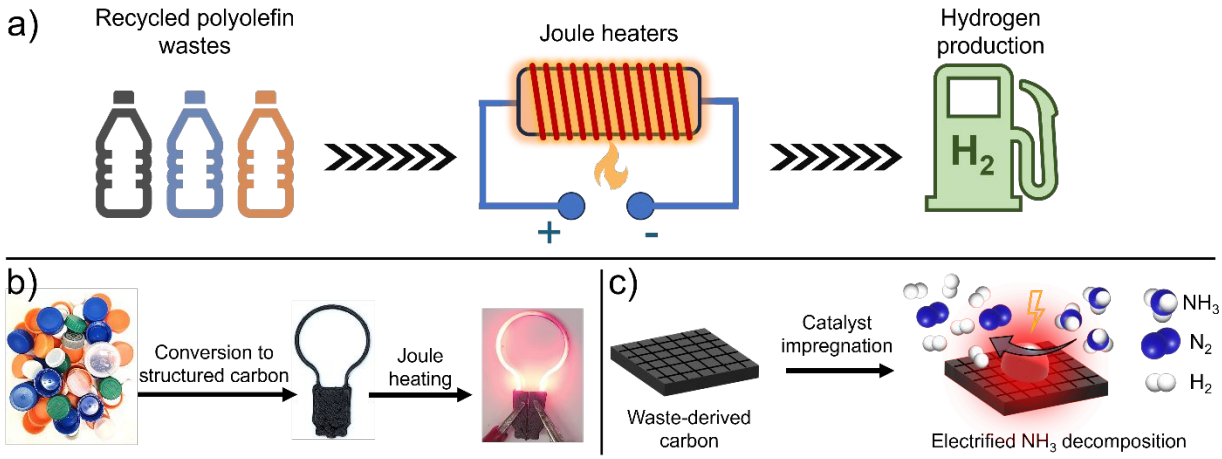

Schematic 1. (a) Illustration demonstrating the upcycling of recycled mixed polyolefin waste to carbon-based Joule heaters for hydrogen production. (b) mixed waste can be collected from single-use plastic bottlecaps, compounded into 3D-printing filament, and FFF-printed into structured parts. Following this, samples were converted into structured carbon and connected to a power source to demonstrate Joule heating capabilities. (c) Waste-derived carbons can be impregnated with Ru-based catalysts for Joule heating-enabled NH_3 decomposition for hydrogen production.

A commercial polyolefin blend with PE majority phase was selected and printed through a fused filament fabrication (FFF) process. As shown in Figure 1a, the sulfonation-induced crosslinking reaction introduces bulky sulfonic acid groups onto the polymeric backbone of both PE and PP, which then homolytically disassociate and result in the installation of unsaturated bonds within the polymer backbone. The alkene groups then continue to react to form

intermolecular radical couplings completing the crosslinking reaction; the formed polyolefin networks can efficiently yield carbon upon pyrolysis. The sulfonation-based crosslinking reaction kinetics was investigated through tracking of the change in degree of crystallinity for both PE and PP portions through DSC measurements (Figure S3 and 1b). The sulfonation reaction leads to a loss in the degree of crystallinity of polyolefins that can be correlated to reaction progression. The starting material of PE/PP blend exhibited two endothermic melting peaks located at approximately 130 °C and 160 °C. The melting peaks from the second heating cycle were then individually integrated and compared to the starting degree of crystallinity of PE and PP. As shown in Figure 1b, both PE and PP exhibited a reduction in crystallinity as a function of reaction time. PE became completely amorphous after 36 h, while PP required 48 h to achieve a fully amorphous morphology. The slower crosslinking kinetics of PP, compared to PE at the same reaction temperature, is attributed to its higher melting temperature which may result in slower diffusion of sulfuric acid within PP domains at a sulfonation reaction temperature of 125 °C. It is worth noting that the reaction temperature required for sufficient crosslinking for this model system (125 °C) is significantly lower than what is required for bulk PP (~150 °C).[30,45] As a comparison, PP-based filaments from a previous study sulfonated at 150 °C required a reaction time of 48 h to completely disrupt crystallinity, whereas samples reacted at 130 °C still exhibited a crystallinity of ~10% after 72 h of reaction. Additionally, the change in the degree of crystallinity as a function of reaction time for additional sulfonation temperatures (115, 135, and 145 °C) are shown in Figure S4a and S4b. In comparison to the model study (125 °C), elevated temperatures (135 and 145 °C) demonstrate faster crosslinking kinetics which shows complete disruption of crystallinity after 24 h of reaction.

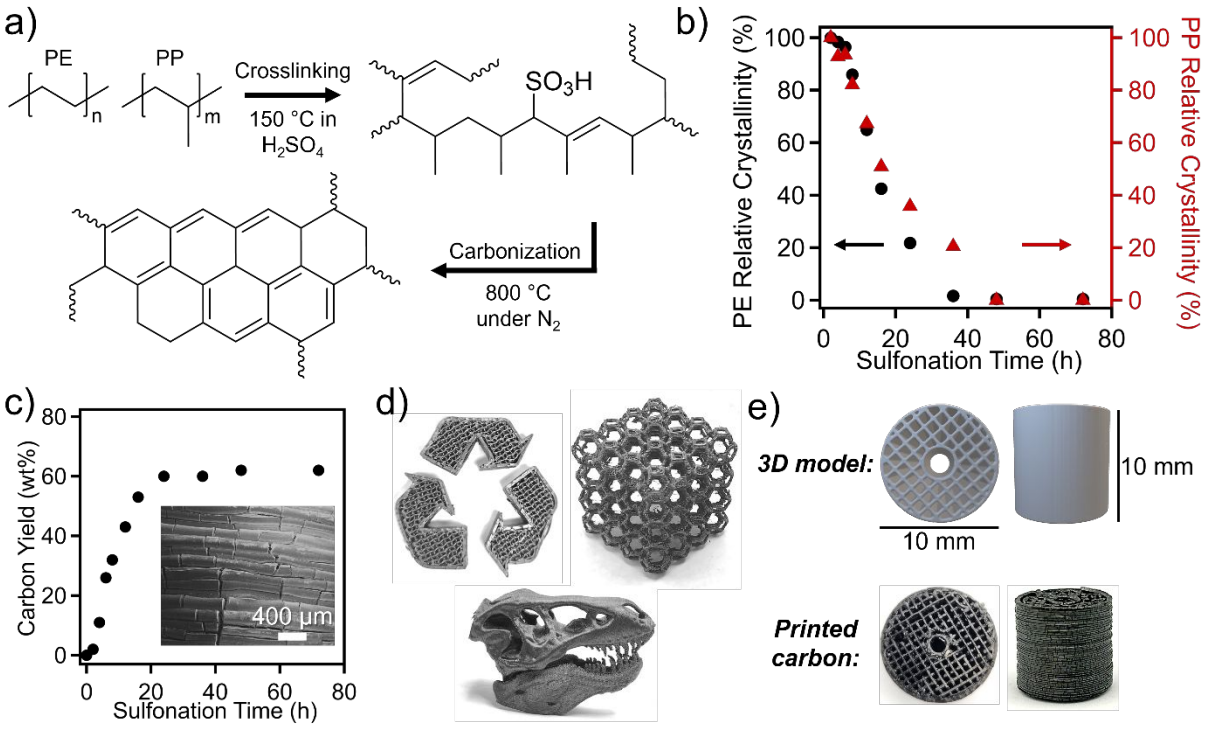

Figure 1. (a) A simplified chemical reaction mechanism of PE and PP undergoing sulfonation-induced interchain crosslinking and subsequent carbonization. (b) Relative degree of crystallinity for PE and PP as a function of sulfonation time at 125 °C for FFF-printed recycled polyolefin. (c)

Carbon yield as a function of sulfonation time for mixed waste-derived carbon with an inset showing an SEM micrograph of the carbon surface for a sample that was sulfonated for 48 h. (d) Demonstration of the attainable complex structures using the reported method. (e) A representative 3D model and image of the corresponding carbon catalyst support.

To further understand the crosslinking kinetics of polyolefins blends, gel fraction measurements were performed as shown in Figure S5, where a steady increase in the insoluble fraction was observed with longer reaction times (19% for 2 h, 31% for 4 h, 55% for 8 h) until a plateau of 91% was reached after 18 h. Furthermore, macroscopic geometry of printed parts was retained following solvent extraction indicating sufficient crosslinking conditions. Additional temperatures (115 °C, 120 °C, 135 °C, 145 °C) were assessed to understand their impact on crosslinking kinetics (Figure S6), while higher temperatures (135 °C and 145 °C) show marginally faster crosslinking kinetics than the model investigation (125 °C). It is important to note that the crosslinking of macrostructured polyolefins is through acid diffusion,[30] where the outer layer of printed structures first undergoes addition of sulfonic acid groups onto the polymeric matrix which changes the property of polyolefin from hydrophobic and hydrophilic. This shift in hydrophilicity leads to differences in acid uptake and swelling between distinct portions within each printed layer. Specifically, the mismatched volume expansion between the outer sulfonated layer and the inner unreacted layer creates local stress, generating micron-sized cracks. These cracks enable further penetration of sulfuric acid, allowing continued crosslinking within the printed structures. The formation of cracks can be examined through SEM in Figure S7, where the printed structure prior to crosslinking has no observable cracks. Following 4 h of reaction time, a few cracks can be observed along printed layer interfaces. With 6 h of reaction time, cracks can be found throughout the structure perpendicular to printed layers and remain consistent with longer reaction times.

Crosslinked structures were then converted into carbon upon pyrolysis, which a maximum carbon yield of ~63 wt% (compared to initial mass of printed structure) was achieved from samples crosslinked for at least 36 h (Figure 1c). The carbon yield for additional reaction temperatures is provided in Figure S8. Figure S9 and the inset in Figure 1c shows SEM of carbons for various crosslinking reaction times, where pyrolysis of samples with very low crosslinking time (2, 4 h) leads to carbon having a complete disruption of macrostructure; increasing reaction times above 4 h enables the retention of macrostructure. Figure S10 shows the dimensional changes of carbon structures compared to their printed dimensions over various reaction times. In-plane shrinkage gradually decreases with increased crosslinking time. Fully crosslinked structures exhibit 17% in-plane shrinkage, consistent with bulk PP-derived carbon structures, and a 2% out-of-plane expansion. It is interesting to note that carbons derived from partially crosslinked polyolefins exhibit slightly greater expansion in the out-of-plane direction and reduced shrinkage upon pyrolysis compared to fully crosslinked samples. To demonstrate the versatility and customizable structure geometry of this carbon manufacturing process, Figure 1d demonstrates the production of various complex shapes of structured carbon, including the universal recycling symbol, a lattice cube, and a tyrannosaurus rex skull. These shapes exhibited consistent shrinkage and carbon yields, similar to the model system (Table S6). The extensive design capabilities provided by AM technology highlight the broad applicability and high scalability of our method for creating 3D structured carbons from recycled polyolefin blends. In comparison to carbon materials with nanoarchitectures, such as nanosheets, core-shell, or fibrous structures,

this 3D-printed polymer-derived carbon method does not require the use of a matrix and can enable reduced pressure drop in flow reaction systems.[46] Therefore, carbon monoliths have been attractive for many research areas, such as electrified heating elements. It is also worth noting that while there are commercially available structured carbons, such as carbon felts derived from cellulose or polyacrylonitrile fibers, attainable geometries remain limited which hinder their potential. Developing complex, customizable structures at scale would allow for the implementation of carbon monoliths into several advanced applications, such as cylindrical catalyst supports for chemical synthesis. Another important consideration is the use of low-cost materials and processes, such as mixed plastic waste and sulfuric acid, in comparison to metal-organic framework-derived carbon nanomaterials or polyacrylonitrile-derived carbon fibers.

Figure 1e shows the 3D models that were used to prepare catalyst support structures as well as images of the structures after carbonization. This cylindrical structure is applicable for their use as catalyst supports, containing a dense grid pattern along the cross-section to facilitate contact between gaseous reactants and carbon walls. To assess the scalability of this process, a series of structures were printed with varied cylinder diameters and lengths. Following carbonization, all samples exhibited consistent carbon yields (~63 wt%) regardless of initial sample geometry and dimensions. The dimensional change results from the printed structure to the final carbon part (Figure S11) indicate the diameter and length of the initial cylinder structure has a minimal impact on the dimension evolution of the final carbon structure, confirming the scalability of our 3D printing carbon process using mixed polyolefins as starting materials.

Additional recycled polyolefin blends were prepared using plastic waste sourced from disposed PE and PP single-use plastics, including mixed wastes with 20, 40, and 80 wt% PP and a 100 wt% PP control. It was found that a higher sulfonation temperature (140 °C) was required for achieving adequate crosslinking for the PP-majority blend than the model PE-majority system. As shown in Figure S12 and S13, it was observed that the relative degree of crystallinity for both PP and PE domains decreased faster with precursors containing greater PE contents. Specifically, a reaction time of 8 h, 12 h, and 24 h resulted in complete disruption of both PE and PP crystallinity for the blends containing 20, 40, and 80 wt% PP, respectively. In comparison, a 100 wt% PP control required 48 h of reaction to disrupt crystallinity. The accelerated crosslinking kinetics of the polyolefin blends can be further characterized through SEM as shown in Figure S14, where all blends exhibit onset of cracking after 2 h of reaction while cracks are not yet observed in the 100 wt% PP control. Following pyrolysis, the recycled polyolefin blends after 36 h of reaction achieved a carbon yield plateau of 73 wt%, 69 wwt%, and 63 wt% for the blends containing 20, 40, and 80 wt% PP, respectively (Figure S15). A 100 wt% PP control exhibited a carbon yield of 57%, which requires 48 h crosslinking time. Retention of cracks within the majority PP blend was also confirmed by SEM image in Figure S16. The versatility of this mixed polyolefin upcycling to structured carbon approach was demonstrated through consistent fabrication of structured carbons from varied waste compositions.

Following preparation of carbon catalyst supports from mixed PE/PP waste, the Joule heating behavior of these samples was first measured in our custom reactor, as shown in Figure 2a including a schematic illustration and photo of the reaction apparatus. To assess heat loss under non-reactive conditions, carbons with varied lengths were loaded to the reactor and their maximum equilibration temperature under Argon (Ar) atmosphere was examined as a function of specific power (the power required to maintain desired temperature of the unit mass of carbon cylinder under flowing of inert). Figure 2b shows the temperature of the cylinder increases

nonlinearly with increasing specific power and the slope decreases with increasing temperature, indicating that the efficiency of heating decreased due to the increased heat loss at higher temperatures. Additionally, from the applied voltage and current (Figure S17), the electrical resistance of the carbon cylinder significantly decreased with increasing temperature, which could also contribute to reduced heating efficiency due to the increased relative power deposition on the electrode. It is observed that the specific power decreased with increasing carbon cylinder length from 5 to 13 mm, suggesting that higher heating efficiency may be achieved from a larger reactor. Moreover, the mixed waste derived-carbons were found to have an electrical conductivity of 5.63 S·m and a specific heat capacity of 0.942 J/(g·K) at 25 °C. We would also like to mention that it is challenging to compare Joule heating efficiency quantitatively with other works as its performance depends highly on both sample geometry and size. However, qualitatively, the carbon Joule heaters from this work exhibit comparable or better heating efficiencies to carbon heaters from several studies, ranging from carbon fiber to 3D-printed carbon.[30,45,47]

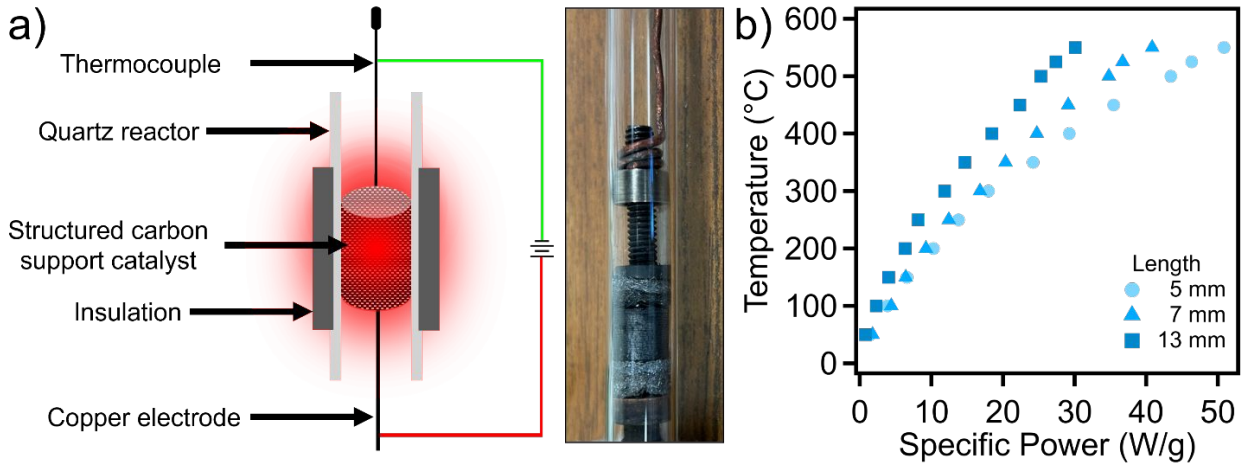

Figure 2. (a) Schematic illustration and image of the Joule-heated reactor setup with carbon catalyst supports. (b) Temperature as a function of specific power for various carbon catalyst support with different length and a diameter of 10 mm.

3.2. Implementation of structured carbons as catalyst supports

Before introducing catalytically active species, carbon cylinders were treated with NH_3 gas at 800 °C for 6 h to remove sulfur heteroatoms doped in their framework. The presence of sulfur heteroatom could influence the structure and surface properties of the catalytically active species. As shown in Figure S18, the pristine carbon supported Ru catalyst shows very low activity and stability in NH_3 decomposition even under conventional thermal catalytic conditions. However, both activity and stability significantly increased after treating the carbon with NH_3 at 800 °C for 6 h. According to XPS measurements (Figure 3a), the pristine carbon has a sulfur content of approximately 0.4 at% and an oxygen content of approximately 5.3 at%. Representative high-resolution XPS scans for the pristine carbon are shown in Figure S19 a-c for carbon, oxygen, and sulfur, respectively. Specifically, the *C 1s* peak can be deconvoluted to three chemical states (C-C sp^2, C-C sp^3, and O-C=O), while the *O 1s* peak can be deconvoluted into two chemical states (C-O and C=O). Lastly, sulfur was observed with a C-S-C $2p_{3/2}$ functionality. As shown in Figure S20 a-d, the peak associated with sulfur heteroatoms disappeared after NH_3 treatment,

meanwhile the oxygen content was reduced to 2.1 at% and a slight amount of nitrogen doping was observed (0.7 at%). We note that minimal change in carbon chemical states is observed following NH_3 treatment, however, *O 1s* is only observed with C-O functionality, indicating the C=O chemical state was removed upon treatment. Additionally, *N 1s* is observed solely in a pyridinic bonding environment. Moreover, both pore volume and surface area (according to liquid nitrogen physisorption; Figure 3b) increased from 0.67 cm^3/g and 520 m^2/g for the pristine carbon to 0.98 cm^3/g and 757 m^2/g after NH_3 treatment. These increases can be attributed to partial activation of the carbon walls upon reacting with NH_3 gas, resulting in enhanced surface area. Additional results about the cumulative pore volume and how pore volume and surface of carbons change as a function of crosslinking times can be found in Figure S21 and S22. The pore size distributions derived from NLDFT models in Figure 3c illustrate the presence of micropores within the carbon framework as well as the broad meso-/macropore population. Several studies have shown that mesopores can form in PP-derived carbons, but this typically requires deliberate undercrosslinking through partial decomposition of the matrix. In our mixed polyolefin system, an averaged pore size of 52 nm was observed following carbonization, which decreased to 46 nm following NH_3 treatment. The slight broadening and decrease in pore size may be due to etching and shrinkage of the carbon framework from exposure to NH_3 at elevated temperatures. The presence of meso-/macropores within carbon framework from fully crosslinked samples can also be confirmed through SEM imaging (Figure S23). This broad macro-mesoporous morphology within the carbon matrix may be beneficial for improved sorption and transport of guest molecules.[48]

After NH_3 treatment, Ru (1 wt%) was introduced to the carbon cylinder through incipient wetness impregnation followed by aqueous phase reduction using $NaBH_4$. Following Ru loading, oxygen content was shown to slightly increase (3.6 at%) and nitrogen content was retained (1.4 at%). As shown in Figure S24 a-c, carbon, oxygen, and nitrogen chemical states remain unaffected following Ru loading. Additionally, the pore volume and surface area decreased slightly to 0.72 cm^3/g and 596 m^2/g, respectively. The reduced pore volume and surface area following Ru loading may be due to nanoparticles infiltrating the micropores within the carbon framework.[49,50] The size and morphology of the Ru nanoparticles supported on the carbon cylinder were then characterized by TEM. As shown in Figure 3d, the simple impregnation method followed by $NaBH_4$ reduction resulted in the uniform formation of spherical Ru nanoparticles with a particle size between 2-5 nm (Figure 3e). Based on the mean particle size of 3 nm, Ru density of 12.2×10^6 g/m^3, and surface area of 0.0613 nm^2 per Ru atom, the Ru dispersion was calculated to be 61%. The high-resolution TEM of a selected nanoparticle demonstrated the presence of 101 planes of the hexagonal close-packed (hcp) Ru (lattice distance of 0.207 nm), which have been frequently identified in the Ru based NH_3 decomposition catalysts.[51] Meanwhile, isolated Ru single atom sites most likely were not formed based on the employed impregnation method according to the High-angle annular dark-field scanning transmission electron microscopy (HAADF-STEM), as shown in Figure S25. Indeed, the single atom Ru sites should be less active in NH_3 decomposition than the nanoparticles due to the significant structure sensitivity (vide infra).

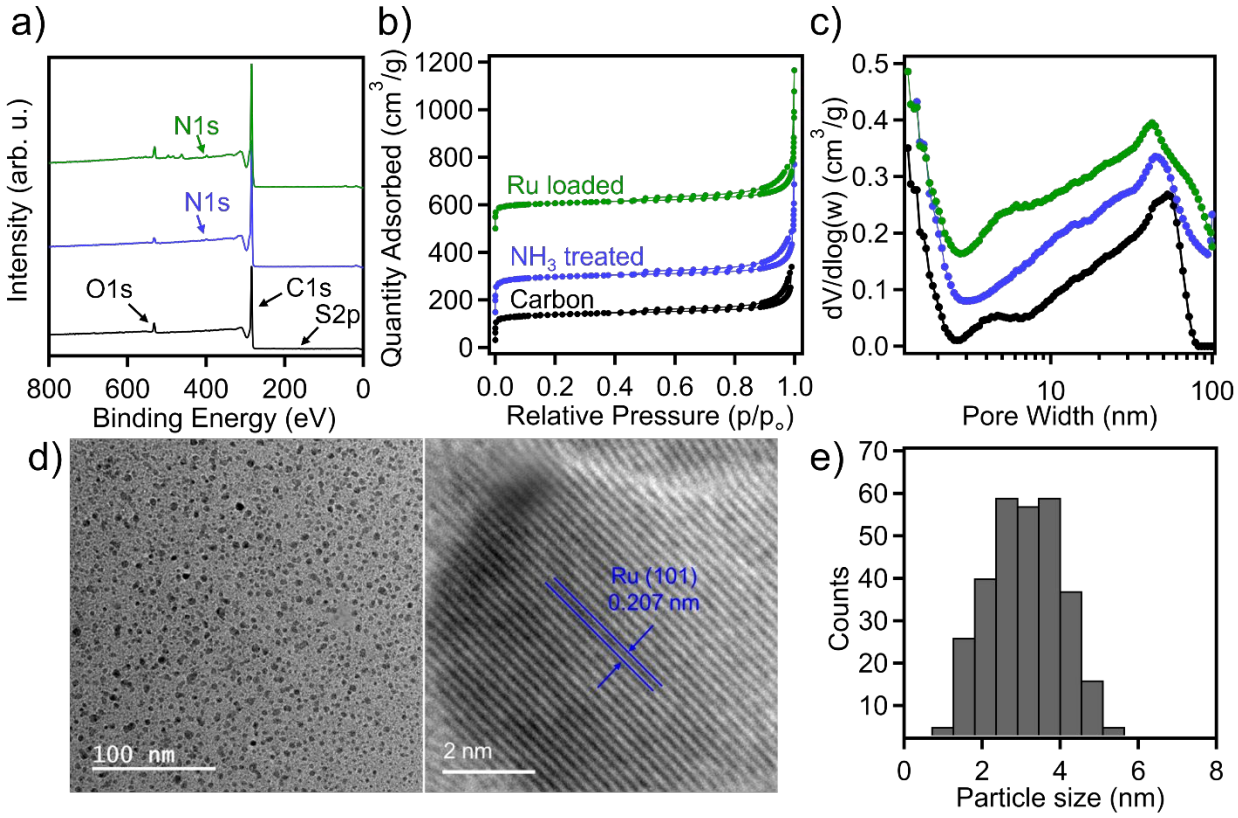

Figure 3. (a) XPS survey scan, (b) nitrogen physisorption isotherm, and (c) associated pore size distribution of 3D printed carbon catalyst support following pyrolysis, NH_3 treatment, and Ru loading. Isotherms were shifted in the positive Y-direction: carbon (+0), NH_3 treatment (+100), and Ru loading (+450). Pore size distributions were shifted in the positive Y-direction: carbon (+0), NH_3 treatment (+0.08), and Ru loading (+0.16). (d) TEM micrograph of carbon cylinder following Ru loading and (e) histogram of Ru particle size.

3.3. Joule-heated catalytic NH_3 decomposition

The Ru-loaded carbon was employed for Joule-heated catalytic NH_3 decomposition using renewable electricity. The catalytic performance of NH_3 decomposition was investigated at temperatures between 400 and 550 °C with space velocities between 33.7 and 84.6 mL/(g min) (using undiluted NH_3 as the feedstock). As shown in Figure 4a, the Ru-loaded carbon is highly active in Joule heating catalytic NH_3 decomposition. The conversion of NH_3 is up to 93% at 550 °C at a low space velocity. Increasing space velocity only slightly decreased the conversion, remaining above 82% at 84.6 mL/(g min) at 550 °C. The conversion of NH_3 decreases significantly with decreasing temperature due to the reduced reaction rate. Noteworthily, the equilibrium conversion of NH_3 decomposition at 400 °C under atmospheric pressure is close to 100%, suggesting that the lower conversion is either kinetically limited or diffusion limited. The rate of H_2 production was calculated from NH_3 conversion to demonstrate the catalytic activity and understand the kinetic behaviors. As shown in Figure 4b, the rate of H_2 production increases significantly with higher temperature and space velocity, reaching up to 70 μmol/(g s) at 550 °C and space velocity of 84.6 mL/(g min). At low temperatures, the rate of H_2 generation is almost

independent of the space velocity, whereas, at higher temperatures the rate increases almost linearly with increasing space velocity (Figure S26). To better understand the reaction kinetic behavior, the Arrhenius plots of the rate of H_2 generation were included in Figure 4c. Significant deviations from the linear Arrhenius behavior were observed at higher temperatures because the reaction is not performed under the differential conditions. These results also suggested that the reaction rate of NH_3 decomposition is related positively to the NH_3 partial pressure, which is in agreement with the kinetic studies of the conventional thermal catalytic NH_3 decomposition where the rate equation is positively related to the NH_3 partial pressure but negatively to the H_2 partial pressure, following the Temkin–Pyzhev mechanism.[52] At temperatures below 475 ºC, linear Arrhenius behaviors were observed for the investigated different space velocities. The apparent activation energy is approximately 80 kJ/mol at space velocities of 67.4 and 84.6 mL/(g min). However, the apparent activation energy slightly decreased with decreasing space velocity from 67.4 to 33.7 mL/(g min), which suggested that the reaction rate is external diffusion-limited due to the lower flow rate. We note that the activation energy of NH_3 decomposition over the Ru-based catalysts was found to range from 90 to 247 kJ/mol from early studies using conventional heating method.[52–58] The activation energies from the Joule heating catalytic NH_3 decomposition are lower than these reported values, most likely due to the electric current effect on the catalysis.[59,60] In the element steps of NH_3 decomposition, the associative desorption of adsorbed N atoms has been considered as the rate-determining step.[54] Therefore, the presence of electric field can enhance the recombinative desorption of N_2 as demonstrated in previous studies.[61]

Noteworthily, the Ru-based catalysts have been extensively studied in order to improve the conventional thermocatalytic activity for NH_3 decomposition at low temperatures and lower Ru loading.[62–67] Table S7 compiled the catalytic performance of various Ru based catalysts for NH_3 decomposition. It can be found that the rates of H_2 production from our study based on the Joule heating catalysis are above the average among the literature (based on the conventional thermocatalytic process) although more detailed comparison of the rate is difficult because the catalyst and reaction conditions are varied among the literatures. The NH_3 decomposition over the Ru catalyst are highly structure sensitive, therefore the activity can be tuned by the particle size and morphology, Ru/support interaction, and promoters. For example, by varying the Ru loading on the Al_2O_3 support, Zheng et al., prepared Ru clusters with mean sizes ranging from 1.9 to 4.6 nm.[68] The NH_3 decomposition over the prepared Ru/Al_2O_3 catalyst was determined to be a structure-sensitive that is best carried out over small Ru particles with size of 2.2 nm. Reducing Ru size below 1.9 nm led to an increase in apparent activation energy and pre-exponential factor. Karim et al. studied the size and shape effect of Ru particles (supported on γ-Al_2O_3) on the activity of NH_3 decomposition.[69] It was found that the particle shape can change from a round one, for smaller particles, to an elongated, flat one, for larger particles. The turnover frequency (TOF) increased by almost 2 orders of magnitude as the particle size increases from 0.8 nm to >7 nm. Yan et al. found that the activity of the Ru in NH_3 decomposition can be tuned by the metal/support interaction.[70] Due to the strong metal–support interactions (SMSI) between Ru and TiO_2, the TOF of NH_3 decomposition on the Ru/TiO_2 is 2-fold higher than that on Ru/SiO_2. Li et al. studied the influence of the porous and graphitic structures of different carbon supports on the activity of Ru for NH_3 decomposition,[71] it was identified that the activity decreases according to the following order: Ru/GC (graphitic carbon) > Ru/CNTs (carbon nanotube) > Ru/CB-S (carbon black) > Ru/CB-C > Ru/CMK-3 $\approx$ Ru/AC. Therefore, we note that there is a potential to further enhance low-temperature NH_3 conversion by optimizing the design of the catalytic active sites, which is our ongoing research.

In terms of power supply, the power-temperature relationships under steady-state Joule-heated catalytic NH_3 decomposition and non-reactive (Ar) atmosphere at different space velocities are shown in Figure 4d. The power input to reach the desired temperature under Ar changes negligibly with changing space velocity, indicating that the sensible heat of Ar has a negligible effect on the heating efficiency. The increased power supply with increasing temperature is due to heat loss rather than the sensible heat effect of the carbon cylinder. During the reaction, the power input is higher than under inert conditions due to reaction endothermicity.

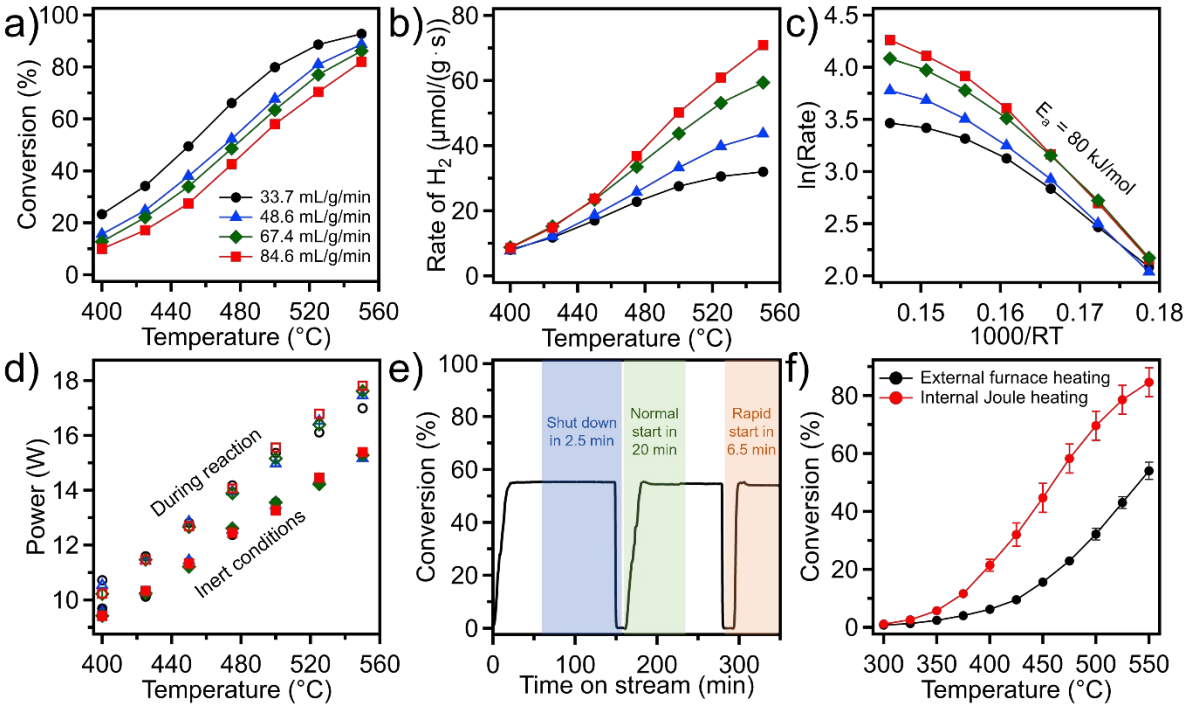

Figure 4. Catalytic performance of Joule heating catalytic NH_3 decomposition. (a) Influence of space velocity on NH_3 conversion and (b) rate of H_2 production; (c) Arrhenius plots of H_2 rate; (d) power input under reaction conditions (open symbols) and inert at the same space velocity; (e) reaction performance under intermittent operation at 450 °C and 33.7 mL/(g min) ("Normal start" means setting the input power to a pre-determined valve and letting the reaction reach the steady state without manual perturbing on the power input, "rapid start" means setting the input power to slightly higher than the pre-determined valve and tuning the power manually to reach the desired temperature); (f) catalytic performance of internal Joule heating in contrast to external furnace heating (error bars were obtained from three different measurements). Catalyst: 1 wt% Ru/C (size of the C cylinder Φ10×h15 mm, mass 0.44 g).

The catalytic performance under different temperatures and space velocities confirms the efficient use of mixed polyolefin waste-derived carbons in Joule heating catalytic system for NH_3 decomposition. A principal advantage of this strategy is that an electrified thermal catalytic system could use intermittent renewable electricity to drive the endothermic NH_3 decomposition, which is a highly efficient tool for power-to-X.[72] The electrified NH_3 decomposition has recently been studied also by nonthermal plasma- and magnetic induction heating-assisted catalysis.[73,74] The Joule heating catalysis shows the highest potential to achieve energy efficiency NH_3 decomposition due to it converts electric energy 100% to heat. To demonstrate the capability of

using renewable electricity for distributed H_2 production, the proposed Joule heating catalytic NH_3 decomposition was further investigated under intermittent conditions. As shown in Figure 4e, the reaction can be turned off within 2.5 min after turning off the power supply. Under the "normal start" conditions, namely, turning on the power to a pre-determined valve without further manual perturbing on the power input, the reaction reaches a steady state within 20 min. If a "rapid start" is performed by setting the input power to slightly higher than the pre-determined value and tuning the power manually to reach the desired temperature, the reaction can reach steady state within only 6.5 min. Such a fast response to the "ON/OFF" operation without influence on the catalytic performance under steady state demonstrates the advantageous capability of using renewable electricity for distributed H_2 production. Figure S27 shows the long-term stability of this Joule-heated catalytic NH_3 decomposition approach enabled through waste-derived carbon, with consistent NH_3 conversion following 1350 min. Another key advantage of our Joule heating catalytic system is that the presence of current and electric field might influence the adsorption, desorption, and activation of the reactants, products, and intermediates, which provides additional possibility to tune the catalytic activity and selectivity.[59] As shown in Figure 4f, the NH_3 conversion during Joule heating catalysis is significantly higher (increased by 50-250% depending on the reaction conditions) than that during the conventional external furnace heated system, demonstrating the positive influence of electric current/field on the catalytic NH_3 decomposition activity. The enhanced activity in NH_3 decomposition is likely related to the decreased activation energy of the associative desorption of chemisorption N atoms in the presence of electric current/field as discussed above. Similar observations on the positive influence of the electric field on the catalytic activity of NH_3 decomposition have been discussed in the literature.[60,61,75]

3.3. LCA of electrified hydrogen production using waste carbon-based Joule heaters

The Joule-heated process for chemical reaction can result in greater energy efficiency than traditional heating methods, thereby reducing overall energy demand. An LCA was conducted to elucidate the holistic life cycle environmental impacts of Joule-heated NH_3 decomposition compared to conventional furnace heating, using base-case (BC) and theoretical minimum (TM) scenarios. Our results indicated that, at lower temperature, Joule heating has lower global warming impact compared to furnace heating (Figure 5a). However, as temperature increases, the BC Joule heating system shows no discernable advantage over furnace heating. This trend is due to the emission factor of the U.S. average electricity mix being larger than that of natural gas heating. Therefore, as energy demand increases per unit conversion, the GHG from Joule and furnace heating will converge. If we consider the favorable scenario where inefficiencies in the lab-scale Joule heating system are eliminated upon scale-up (the TM scenario), Joule heating can lead to more than a 200% reduction in Global warming potential (GWP)100 impact at all temperatures.

To understand the optimal conditions to run the Joule heated reactor, we measured conversion for a range of ammonia feed flow rates and temperatures. GWP100 impact for the BC Joule heated reactor for each of these flow rates and temperatures was simulated (Figure 5b). The lowest GWP100 impact was determined to be at ~30 mL/min and ~500 ºC, with a conversion reaching 63%. This result highlights the trade-offs between conversion, amount of hydrogen produced, and energy required. As more energy is consumed to complete the reaction, GWP100 impact will decrease as conversion increases until a point where the additional hydrogen

produced no longer offsets the increased emissions from heating. The exact optimal operating point will shift based on the reactor performance and the carbon intensity of the electric grid used.

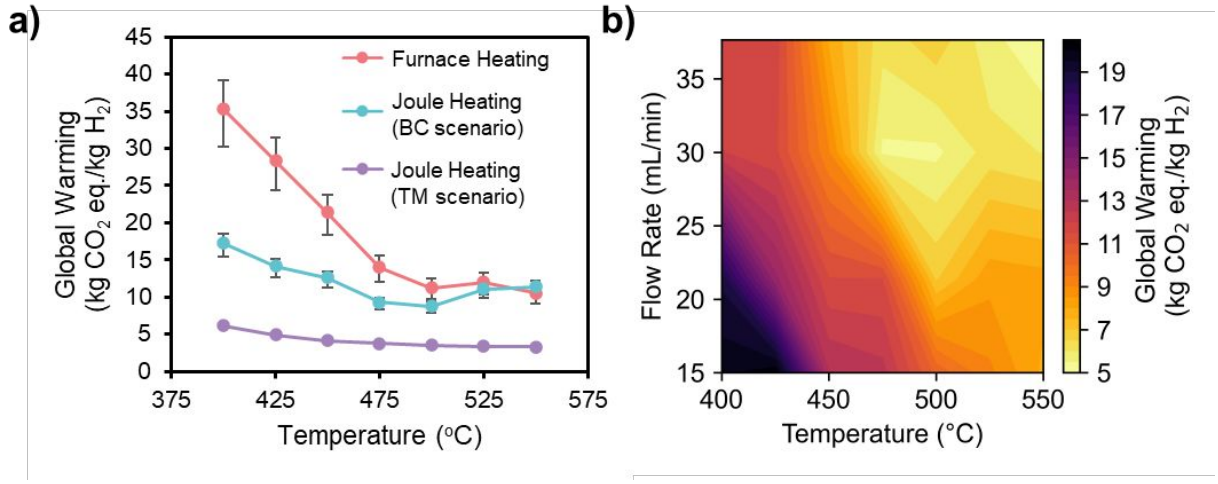

Figure 5. (a) The global warming impact of furnace heating and Joule heating for ammonia decomposition at different temperatures. Joule heating impact was calculated for two scenarios that approximate the possible upper (base-case (BC) scenario) and lower (theoretical minimum (TM) scenario) bounds for performance of the technology at industrial-scale. Error bars represent the uncertainty in reported industrial heat efficiencies of each heating technology. (b) A contour plot showing the global warming impact of BC Joule heating at various ammonia feed flow rates and reaction temperatures. The optimal operating temperature and flow rate are identified to minimize GWP.

Considering that the environmental impact is driven by energy consumption, the electricity source used for Joule heating is crucial. As grids transition to renewable energy, Joule heating is expected to become more environmentally sustainable. Figure 6 illustrates how increasing shares of different energy sources could impact GWP100 impact and life cycle energy consumption (LCEC) of Joule heating. For this analysis, we considered the BC scenario to calculate electricity usage, and that the reactor was operated under the optimal conditions found in Figure 5b (NH_3 feed rate of 30 mL/min and temperature of 500ºC). The 2020 U.S. average electricity grid mix consists of approximately 41% natural gas, 19% coal, 20% nuclear, and 20% from renewable sources such as wind, solar, and hydro.[37] Figure 6a shows how transitioning the U.S. electric grid to renewable energy sources can lead to, approximately, a more than 400% decrease in GWP100 impact in Joule heating. Of these energy sources, nuclear and hydroelectric power show the greatest decrease in GWP100 impact (0.13 and 0.11 kg CO_2 eq./kg H_2, respectively). Figure 6b shows that transitioning to clean energy leads to approximately 200% decrease in the total LCEC of the Joule heating process. This LCEC indicator accounts for all the energy required in construction and operation of each electricity production technology, which can help decision makers understand how the implementation of Joule heating may strain existing electric grids. If we consider a best-case scenario using only hydroelectric power calculated considering the TM scenario, GWP100 impact and LCEC can be as low as 0.05 kg CO_2 eq./kg H_2 and 33 MJ eq./kg H_2, respectively. This best-case Joule heating impact greatly outclasses the conventional furnace technology with GW impact and LCEC of 11.3 and 199, respectively. LCA results for all other impact categories (eutrophication, acidification, etc.) can be found in Section S2.2 and Figures S28 and S29.

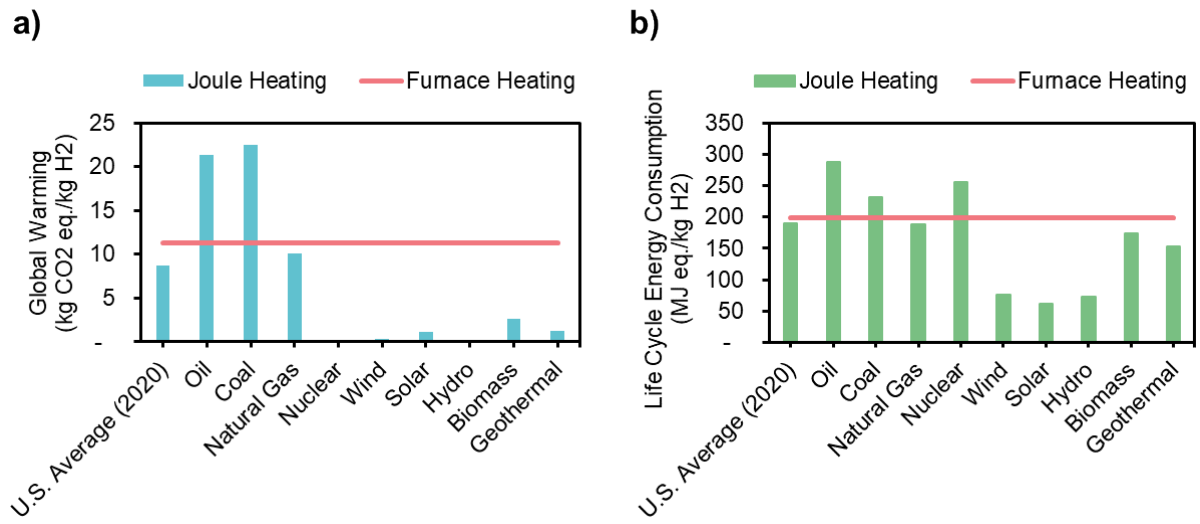

Figure 6. (a) The global warming impact of ammonia decomposition by Joule heating (blue bars) versus conventional furnace heating (red line) for various energy sources. (b) The life cycle energy consumption (LCEC) of ammonia decomposition by Joule heating (green bars) versus conventional furnace heating (red line) for various energy sources.

4. Conclusions

This work demonstrates the upcycling of mixed polyolefin waste into 3D-structured carbons with outstanding Joule heating properties, which can be directly utilized as catalyst supports for the electrified hydrogen production. It is found that the Joule-heating enabled decomposition of NH_3 achieved enhanced conversion when compared to conventional thermal heating, in addition to exhibiting accelerated startup and shutdown speeds. The versatility of this simple upcycling strategy was demonstrated through generalizing mixed polyolefin waste precursors to a majority PP composition, where no detrimental impact on their conversion to carbon or their use in electrified chemical synthesis was observed. Additionally, Joule heating showed reduced GHG and LCEC impact (8.78 kg CO_2 eq./kg H_2 and 190 MJ eq./kg H_2, respectively) compared to conventional furnace heating (11.3 kg CO_2 eq./kg H_2 and 199 eq./kg H_2, respectively) using the base case scenario and the U.S. average electric grid mix. Transitioning to more renewable energy could decrease GHG by around 400% and LCEC by 200%. This work presents a scalable strategy to convert mixed waste feedstocks into structured carbons suitable for electrified chemical synthesis addressing several challenges simultaneously, including AM of carbonaceous materials, plastic waste upcycling, electrified chemical synthesis, and carbon-zero fuel production.

5. Acknowledgements

This project was partially supported by the National Science Foundation (CMMI-2239408, ECO-CBET 2133530, OIA) and the Mississippi SMART Business Act.

6. Conflicts of interests

The authors declare the following competing interests: Z.Q. and P.S. submitted two U.S. patent applications for relevant technology of AM of carbons (U.S. Application No. 17/848,342; No. 18/112,446). The remaining authors declare no competing interests.

7. Data Availability

The data supporting this study are available upon request from the corresponding author.

8. References

1 F. Vidal, E. R. van der Marel, R. W. F. Kerr, C. McElroy, N. Schroeder, C. Mitchell, G. Rosetto, T. T. D. Chen, R. M. Bailey, C. Hepburn, C. Redgwell and C. K. Williams, *Nature*, 2024, **626**, 45–57.

2 L. T. J. Korley, T. H. Epps, B. A. Helms and A. J. Ryan, *Science*, 2021, **373**, 66–69.

3 T.-W. Lin, O. Padilla-Vélez, P. Kaewdeewong, A. M. LaPointe, G. W. Coates and J. M. Eagan, *Chem. Rev.*, 2024, **124**, 9609–9632.

4 K. P. Sullivan, A. Z. Werner, K. J. Ramirez, L. D. Ellis, J. R. Bussard, B. A. Black, D. G. Brandner, F. Bratti, B. L. Buss, X. Dong, S. J. Haugen, M. A. Ingraham, M. O. Konev, W. E. Michener, J. Miscall, I. Pardo, S. P. Woodworth, A. M. Guss, Y. Román-Leshkov, S. S. Stahl and G. T. Beckham, *Science*, 2022, **378**, 207–211.

5 Z. Xu, N. E. Munyaneza, Q. Zhang, M. Sun, C. Posada, P. Venturo, N. A. Rorrer, J. Miscall, B. G. Sumpter and G. Liu, *Science*, 2023, **381**, 666–671.

6 L. D. Ellis, N. A. Rorrer, K. P. Sullivan, M. Otto, J. E. McGeehan, Y. Román-Leshkov, N. Wierckx and G. T. Beckham, *Nat. Catal.*, 2021, **4**, 539–556.

7 J. Qian, C.B. Dunn, and Z. Qiang *Macromol. Chem. Phys.*, 2023, **224**, 2300291.

8 Q. Dong, A. D. Lele, X. Zhao, S. Li, S. Cheng, Y. Wang, M. Cui, M. Guo, A. H. Brozena, Y. Lin, T. Li, L. Xu, A. Qi, I. G. Kevrekidis, J. Mei, X. Pan, D. Liu, Y. Ju and L. Hu, *Nature*, 2023, **616**, 488–494.

9 B. Shirizadeh, A. Ailleret, A. Guillon, E. Bovari, N. El Khatib, S. Douguet, C. B. Issa, J. Brauer and J. Trüby, *Energy Environ. Sci.*, 2023, **16**, 6094–6109.

10 A. Klerke, C. H. Christensen, J. K. Nørskov and T. Vegge, *J. Mater. Chem.*, 2008, **18**, 2304–2310.

11 K. E. Lamb, M. D. Dolan and D. F. Kennedy, *Int. J. Hydrogen Energy*, 2019, **44**, 3580–3593.

12 S. Sun, Q. Jiang, D. Zhao, T. Cao, H. Sha, C. Zhang, H. Song and Z. Da, *Renew. Sustain. Energy Rev.*, 2022, **169**, 112918.

13 C. M. Woodall, Z. Fan, Y. Lou, A. Bhardwaj, A. Khatri, M. Agrawal, C. F. McCormick and S. J. Friedmann, *Joule*, 2022, **6**, 2474–2499.

14 D. S. Mallapragada, Y. Dvorkin, M. A. Modestino, D. V. Esposito, W. A. Smith, B.-M. Hodge, M. P. Harold, V. M. Donnelly, A. Nuz, C. Bloomquist, K. Baker, L. C. Grabow, Y. Yan, N. N. Rajput, R. L. Hartman, E. J. Biddinger, E. S. Aydil and A. D. Taylor, *Joule*, 2023, **7**, 23–41.

15 S. T. Wismann, J. S. Engbæk, S. B. Vendelbo, F. B. Bendixen, W. L. Eriksen, K. Aasberg-Petersen, C. Frandsen, I. Chorkendorff and P. M. Mortensen, *Science*, 2019, **364**, 756–759.

16 S. T. Wismann, J. S. Engbæk, S. B. Vendelbo, W. L. Eriksen, C. Frandsen, P. M. Mortensen and I. Chorkendorff, *Chem. Eng. J.*, 2021, **425**, 131509.

17 Q. Dong, Y. Yao, S. Cheng, K. Alexopoulos, J. Gao, S. Srinivas, Y. Wang, Y. Pei, C. Zheng, A. H. Brozena, H. Zhao, X. Wang, H. E. Toraman, B. Yang, I. G. Kevrekidis, Y. Ju, D. G. Vlachos, D. Liu and L. Hu, *Nature*, 2022, **605**, 470–476.

18 Y. Li, S. Zuo, F. Wei, C. Chen, G. Zhang, X. Zhao, Z. Wu, S. Wang, W. Zhou, M. Rueping, Y. Han and H. Zhang, *Proc. Natl. Acad. Sci. U.S.A.*, 2024, **121**, e2315362121.
19 H. Zhang, W. Zhou, X. F. Lu, T. Chen and X. W. (David) Lou, *Adv. Energy Mater.*, 2020, **10**, 2000882.
20 Z.-L. Wang, K. Sun, J. Henzie, X. Hao, C. Li, T. Takei, Y.-M. Kang and Y. Yamauchi, *Angew. Chem. Int. Ed.*, 2018, **57**, 5848–5852.
21 T. Jiang, Z. Liu, Y. Yuan, X. Zheng, S. Park, S. Wei, L. Li, Y. Ma, S. Liu, J. Chen, Z. Zhu, Y. Meng, K. Li, J. Sun, Q. Peng and W. Chen, *Adv. Mater.*, 2023, **35**, 2300502.
22 J. Chen, Y. Ma, T. Huang, T. Jiang, S. Park, J. Xu, X. Wang, Q. Peng, S. Liu, G. Wang and W. Chen, *Adv. Mater.*, 2024, **36**, 2312369.
23 K. Yu, C. Wang, W. Zheng and D. G. Vlachos, *ACS Energy Lett.*, 2023, **8**, 1050–1057.
24 D. X. Luong, K. V. Bets, W. A. Algozeeb, M. G. Stanford, C. Kittrell, W. Chen, R. V. Salvatierra, M. Ren, E. A. McHugh, P. A. Advincula, Z. Wang, M. Bhatt, H. Guo, V. Mancevski, R. Shahsavari, B. I. Yakobson and J. M. Tour, *Nature*, 2020, **577**, 647–651.
25 W. Chen, J. T. Li, Z. Wang, W. A. Algozeeb, D. X. Luong, C. Kittrell, E. A. McHugh, P. A. Advincula, K. M. Wyss, J. L. Beckham, M. G. Stanford, B. Jiang and J. M. Tour, *ACS Nano*, 2021, **15**, 11158–11167.
26 J. Ahn, S. Park, D. Oh, Y. Lim, J. S. Nam, J. Kim, W. Jung and I.-D. Kim, *ACS Nano*, 2023, **17**, 12188–12199.
27 B. Deng, Z. Wang, W. Chen, J. T. Li, D. X. Luong, R. A. Carter, G. Gao, B. I. Yakobson, Y. Zhao and J. M. Tour, *Nat. Commun.*, 2022, **13**, 262.
28 H. Yang, I. Nuran Zaini, R. Pan, Y. Jin, Y. Wang, L. Li, J. J. B. Caballero, Z. Shi, Y. Subasi, A. Nurdiawati, S. Wang, Y. Shen, T. Wang, Y. Wang, L. Sandström, P. G. Jönsson, W. Yang and T. Han, *Nat. Commun.*, 2024, **15**, 3868.
29 A. Griffin, M. Robertson, Z. Gunter, A. Coronado, Y. Xiang and Z. Qiang, *Ind. Eng. Chem. Res.*, 2024, **63**, 19398–19417.
30 P. Smith, A. G. Obando, A. Griffin, M. Robertson, E. Bounds and Z. Qiang, *Adv. Mater.*, 2023, **35**, 2208029.
31 P. Smith, J. Hu, A. Griffin, M. Robertson, A. Güillen Obando, E. Bounds, C. B. Dunn, C. Ye, L. Liu and Z. Qiang, *Nat. Commun.*, 2024, **15**, 838.
32 J. D. Menczel and R. B. Prime, *Thermal Analysis of Polymers: Fundamentals and Applications*, John Wiley and Sons, 2008.
33 E. J. Clark and Hoffman, *Macromolecules*, 1984, **17**, 878–885.
34 *Environmental management: Life cycle assessment; Principles and framework; International Organization for Standardization*, 2006.
35 *Environmental management: Life cycle assessment; Requirements and guidelines; International Organization for Standardization*, 2006.
36 G. Wernet, C. Bauer, B. Steubing, J. Reinhard, E. Moreno-Ruiz and B. Weidema, *Int. J. Life Cycle Assess.*, 2016, **21**, 1218–1230.
37 *Electricity in the U.S. - U.S. Energy Information Administration (EIA)*.
38 J. Bare, *Clean. Technol. Environ. Policy*, 2011, **13**, 687–696.
39 R. Hischier, B. Weidema, H.-J. Althaus, C. Bauer, G. Doka, R. Dones, R. Frischknecht, S. Hellweg, S. Humbert, N. Jungbluth, T. Koellner, Y. Loerincik, M. Margni and T. Nemecek, *Implementation of Life Cycle Impact Assessment Methods. ecoinvent report No. 3, v2.2*, 2010.
40 S. Lupi, *Fundamentals of electroheat*, Springer, Switzerland, 2017.
41 C. O. M. dos Santos, J. M. Botero, K. West and T. Apeldoorn, *Pathways to Industrial Decarbonisation in the Netherlands: Paper & Board and Steam Cracking*, TNO, 2021.
42 W. D. Seider, D. R. Lewin, J. D. Seader, S. Widagdo, R. Gani and K. M. Ng, *Product and Process Design Principles: Synthesis, Analysis, and Evaluation*, John Wiley & Sons, 2017.

43 L. Liu, A. Bhowmick, S. Cheng, B. H. Blazquez, Y. Pan, J. Zhang, Y. Zhang, Y. Shu, D. T. Tran, Y. Luo, M. Ierapetritou, C. Zhang and D. Liu, *Cell. Rep. Phys. Sci.*, 2023, **4**, 101692.
44 J. M. Eagan, J. Xu, R. Di Girolamo, C. M. Thurber, C. W. Macosko, A. M. LaPointe, F. S. Bates and G. W. Coates, *Science*, 2017, **355**, 814–816.
45 A. Griffin, P. Smith, P. Frame, K. Jones and Z. Qiang, *Adv. Sustainable Syst*, 2024, **8**, 2300332.
46 Y. Li, S. Chen, X. Cai, J. Hong, X. Wu, Y. Xu, J. Zou and B. H. Chen, *J. Mater. Chem. A*, 2018, **6**, 5695–5702.
47 W. H. Lee, X. Zhang, S. Banerjee, C. W. Jones, M. J. Realff and R. P. Lively, *Joule*, 2023, **7**, 1241–1259.
48 A. Griffin, M. Robertson, P. Frame, G. Ma, K. A. Green, Z. Han, S. E. Morgan, X. Gu, M. Wang and Z. Qiang, *J. Mater. Chem. A*, 2024, **12**, 13139–13152.
49 M. Robertson, A. Barbour, A. Griffin, J. Aguinaga, D. Patton, Y. Xiang and Z. Qiang, *J. Mater. Chem. A*, 2024, **12**, 17229–17242.
50 A. Griffin, N. Smith, M. Robertson, B. Nunez, J. McCraw, H. Chen and Z. Qiang, *J. Chem. Educ.*, 2024, **101**, 1096–1105.
51 K. C. Leung, E. Tan, G. Li, B. K. Y. Ng, P.-L. Ho, K. Lebedev and S. C. E. Tsang, *Faraday Discuss.*, 2023, **243**, 520–548.
52 M. C. J. Bradford, P. E. Fanning and M. A. Vannice, *J. Catal.*, 1997, **172**, 479–484.
53 W. Tsai and W. H. Weinberg, *J. Phys. Chem.*, 1987, **91**, 5302–5307.
54 C. Egawa, T. Nishida, S. Naito and K. Tamaru, *J. Chem. Soc., Faraday Trans. 1*, 1984, **80**, 1595–1604.
55 S. R. Logan and C. Kemball, *Trans. Faraday Soc.*, 1960, **56**, 144–153.
56 A. Amano and H. Taylor, *J. Am. Chem. Soc.*, 1954, **76**, 4201–4204.
57 S. Kiperman, *J. Phys. Chem. (USSR)*, 1947, **21**, 1435.
58 A. Vitvitskii, T. Gaidei, M. Toporkova and E. Kiseleva, *J. Appl. Chem. (USSR)*, 1990, **63**, 1883.
59 F. Che, J. T. Gray, S. Ha, N. Kruse, S. L. Scott and J.-S. McEwen, *ACS Catal.*, 2018, **8**, 5153–5174.
60 V. Maslova, E. Fourré, G. Veryasov, N. Nesterenko, A. Grishin, C. Louste, M. Nassar, N. Guignard, S. Arrii and C. Batiot-Dupeyrat, *ChemCatChem*, 2023, **15**, e202201626.
61 M. L. T. Triviño, S. Doi, Y. S. Kang, C. U. Lee, Y. Sekine and J. G. Seo, *Chem. Eng. J.*, 2023, **476**, 146715.
62 C. Chen, K. Wu, H. Ren, C. Zhou, Y. Luo, L. Lin, C. Au and L. Jiang, *Energy Fuels*, 2021, **35**, 11693–11706.
63 J. Chen, Z. H. Zhu, S. Wang, Q. Ma, V. Rudolph and G. Q. Lu, *Chem. Eng. J.*, 2010, **156**, 404–410.
64 F. R. García-García, J. Álvarez-Rodríguez, I. Rodríguez-Ramos and A. Guerrero-Ruiz, *Carbon*, 2010, **48**, 267–276.
65 T. E. Bell, G. Zhan, K. Wu, H. C. Zeng and L. Torrente-Murciano, *Top. Catal.*, 2017, **60**, 1251–1259.
66 A. K. Hill and L. Torrente-Murciano, *Int. J. Hydrogen Energy*, 2014, **39**, 7646–7654.
67 S. Armenise, L. Roldán, Y. Marco, A. Monzón and E. García-Bordejé, *J. Phys. Chem. C*, 2012, **116**, 26385–26395.
68 W. Zheng, J. Zhang, H. Xu and W. Li, *Catal. Lett.*, 2007, **119**, 311–318.
69 A. M. Karim, V. Prasad, G. Mpourmpakis, W. W. Lonergan, A. I. Frenkel, J. G. Chen and D. G. Vlachos, *J. Am. Chem. Soc.*, 2009, **131**, 12230–12239.
70 W. Yan, B. Liang, G. Bi, H. Zhuo, W. Wang, H. Duan, G. Xu, F. Wang, Y. Su, T. Zhang, X. Yang and Y. Huang, *ACS Sustainable Chem. Eng.*, 2024, **12**, 15024–15032.
71 L. Li, Z. H. Zhu, Z. F. Yan, G. Q. Lu and L. Rintoul, *Appl. Catal. A Gen.*, 2007, **320**, 166–172.
72 A. R. Dahiru, A. Vuokila and M. Huuhtanen, *J. Energy Storage*, 2022, **56**, 105861.

73 M. R. Shawon, C. Umeojiakor, A. Griffin, J. Aguinaga, J. Wu, D. Patton, Z. Qiang, H. Toghiani and Y. Xiang, *React. Chem. Eng.*, 2025, **10**, 320–331.
74 R. Zhang, X. Liu, N. Song, J. He, Z. Cen, C. Li, M. Wang, H. Tang, W. Liu, X. Ren and D. Ma, *J. Am. Chem. Soc.*, 2024, **146**, 28635–28641.
75 D. Vladov, VL. Dyakovitch and SH. Dinkov, *J. Catal.*, 1966, **5**, 412–418.